** XRD indicate that products synthesized are probably not at equilibrium to declare what the composition of the product actually is
Cs_2AgBiI_6' XRD does not verify if the double perovskite phase is presence or exactly what phases are presence

IV. Conclusions

The phase diagrams help serve as a visual tool of the construction of the halide double perovskite phases by noting all the different product combinations that are possible during its synthesis. It is important to note the movement between one phase to another and how the iodine phase diagram differs from the chlorine, bromine, diagrams. Iodine has many more Ag products, as iodine is very large, soft, and polarizable this may contribute to its difficulty in forming the double perovskite where the different sites need to match a certain size ratio. However, the red product does show promise in the correct band gab direction so perhaps using Bruker D8 for the XRD may help see what peaks are not accounted for. Overall, heating the products between 48-72 hours yielded the purist XRDs. H_3PO_4 is critical for the dissolution of the chlorine's 3-2-9 allowing for the most pure double perovskite sample.

For future work, looking at the crystal structure between the 3-2-9's of the chlorines and bromine contrasts to the iodine's 3-2-9 crystal structures may indicate that the iodine double perovskite may not be possible. Work also needs to be done on all the phase diagrams at testing points in the middle of the system that include all four elements that make up the double perovskite phase. In addition, the crystal structures are in the process of being solved for all blue points on the diagram [$AgBiBr_4$, Cs_3BiBr_6, $AgBi_2I_7$] with most space groups picked out and Wyckoff sites being tested. All gray points should be re-heated to a higher temperature as seen mainly in the iodine system to verify the system is at equilibrium. Overall these phase diagrams provide a data bank for future work done on halide double perovskite systems.

V. Acknowledgments

Thank you to the summer Woodward Group for all their help and guidance in the lab. I want to specifically thank my graduate mentor Eric McClure for giving me the tools for summer research, and for all his previous work done on halide double perovskites. In addition to Dr. Pat Woodward for his mentorship and guidance on how to ask rigorous questions and finding a research direction.

I would also like to thank CEM and the REU program and NSF Materials Research Science and Engineering Center (MRSEC) supported under NSF Award Number DMR-1420451.

VI. Footnotes, Endnotes and References

References

(1) Stranks, S. D.; Snaith, H. J. Metal-Halide Perovskites for Photovoltaic and Light-Emitting Devices. *Nat. Publ. Gr.* **2015**, *10* (5), 391–402.

(2) Stoumpos, C. C.; Malliakas, C. D.; Kanatzidis, M. G. Semiconducting Tin and Lead Iodide Perovskites with Organic Cations: Phase Transitions, High Mobilities, and Near-Infrared Photoluminescent Properties. **2013**.

(3) Volonakis, G.; Filip, M. R.; Haghighirad, A. A.; Sakai, N.; Wenger, B.; Snaith, H. J.; Giustino, F. Lead-Free Halide Double Perovskites via Heterovalent Substitution of Noble Metals. **2016**.

(4) McClure, E. T.; Ball, M. R.; Windl, W.; Woodward, P. M. Cs 2 AgBiX 6 (X = Br, Cl): New Visible Light Absorbing, Lead-Free Halide Perovskite Semiconductors. *Chem. Mater.* **2016**, *28* (5), 1348–1354.

(5) Ternary Phase Diagrams. In *Phase Diagrams- Understanding the Basicss*; Campbell, F. ., Ed.;

ASM International, 2012; pp 1–10.
(6) Hull, S.; Berastegui, P. Crystal Structures and Ionic Conductivities of Ternary Derivatives of the Silver and Copper Monohalides — II : Ordered Phases within the (Ag X) X –(MX) 1 À X and (Cu X) X –(MX) 1 À X (M = K , Rb and Cs ; X = Cl , Br and I) Systems. **2004**, *177*, 3156–3173.
(7) Nowogrocki, G. U. Y.; Thomas, D. Structural Studies of Cs-K-Bi Mixed Chlorides Relation to the Crystal Structures. **1986**, *26*, 13–26.
(8) B., D. C. PREDICTION OF PHASE FORMATION SYSTEMS MI M BIG3. *Proc. Russ. State Pedagog. Univ. AI Herzen* **2004**, *4* (8), 94–99.
(9) Blasse, G. The Luminescence of Cs3Bi2C19 and Cs3Sb2C19. **1983**, *233*, 222–233.
(10) Dzeranova K.B., Kaloev N.I., Egerev O.I., B. G. . Equilibrium Diagram of the BiI3 -CsI System. *J. Inorg. Chem. (translated from Zhurnal Neorg. Khimii)* **1984**, *29*, 1984.
(11) Mashadieva, L. F.; Aliev, Z. S.; Shevelkov, A. V; Babanly, M. B. Experimental Investigation of the Ag – Bi – I Ternary System and Thermodynamic Properties of the Ternary Phases. *J. Alloys Compd.* **2013**, *551*, 512–520.
(12) Atkinson, A. W.; Inorganic, T. Compound Formation Between Indium Trichloride and Other Metal Chlorides. **1970**, *32* (1964).
(13) The, I. N. Preparation of Cubic Chloro Complex Compounds of Trivalent Metals: Cs2NaMCl6. **1969**, *9* (7), 1771–1775.
(14) Groznetskii V.V., Zhuravlev V.D., Kitaev G.A., Z. L. . AgCl-AgBr System. *J. Inorg. Chem. (translated from Zhurnal Neorg. Khimii)* **1985**, *30*, 582–583.

Summer REU Project: Magnetic Skyrmions in Epitaxial Films

Jordan Fuhrman[1], Keng-Yuan (Mark) Meng[2], James Gallagher[2], Fengyuan Yang[2]
[1]*University of Alabama, Department of Physics and Astronomy*
[2]*The Ohio State University, Department of Physics*

ABSTRACT

In magnetic information storage systems, the ability to manipulate magnetic structures is paramount. The skyrmion, a vortex of spins, is one candidate for the improvement of information processing[1-3]. Skyrmions have been observed in some B20 phase crystals, including FeGe, due to the non-symmetric structure of the B20 lattice. Additionally, FeGe thin films have a larger skyrmion phase range than their bulk FeGe crystal counterparts[1]. This skyrmion phase can be detected through the topological Hall effect. Previous studies have shown that the current density must exceed a critical value in order to cause depinning, or motion, of the skyrmion[4]. This project focuses on analyzing the relationship between the topological Hall effect, critical current density for skyrmion motion, and the thickness of the films. The FeGe films are produced using off-axis magnetron sputtering, and are then characterized using both X-ray diffraction and Hall measurements. In order to observe this phenomenon at low current densities, this project employs the use of lock-in technique to achieve increased sensitivity of the topological Hall measurements. These measurements could be valuable for utilizing FeGe thin films in low energy cost spintronic applications.

I. Background and Introduction

Magnetic skyrmions are vortex-like spin textures that can form in chiral magnets.[1,2,5-8] Skyrmions have been noted as potential candidates for improving magnetic information storage technology because of their attractive magnetic qualities.[1-3] Skyrmions have been confirmed by Lorentz TEM images in some B20 phase materials, such as FeGe and MnSi.[7] Skyrmions exist in these materials due to the non-centrosymmetric cubic structure of the B20 phase. This particular structure causes multiple different interactions to compete with each other: long range magnetic dipole interactions, the Heisenberg interaction, and the Dzyaloshinskii-Moriya interaction (DMI). These interactions allow non-collinear magnetic spin alignment, or the formation of skyrmions.[1,10,11] Additionally, the direction of the vortex of each skyrmion is determined by the sign of the DMI, which is governed by the chirality of the crystal.[4]

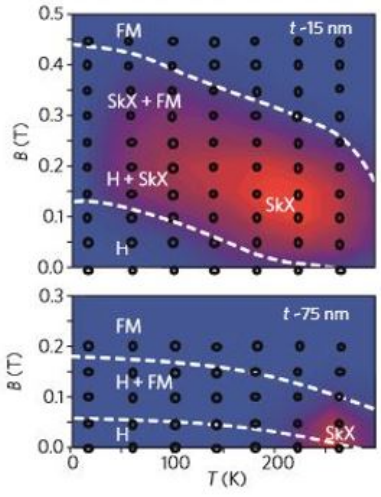

Source: Nagaosa, N. & Tokura, Y. Topological properties and dynamics of magnetic skyrmions. Nat. Nanotechnol. 8, 899–911 (2013).

The motivation for utilizing skyrmions in magnetic information storage is that the current density, and thus the power, required to manipulate the skyrmion crystal is significantly lower than their ferromagnetic domain wall counterparts. Specifically, skyrmions in both MnSi and FeGe have been found to require a current density ~ 10^5 times lower than those needed for ferromagnetic domains.[4,12] Additionally, it is important to include the temperature dependence when considering the applicable possibilities of skyrmion drift. In this regard, FeGe thin films are more promising than MnSi. Low current density skyrmion drift in MnSi has only been observed at relatively low temperatures (26 – 28 K) while the same phenomenon can be observed in FeGe near room temperature.[4]

As an electrical current is passed through an FeGe thin film, a Hall voltage can be measured when there is external magnetic field, resulting in the ordinary Hall effect, and when there is magnetization, resulting in the Anomalous Hall effect. However, when skyrmions are present, this Hall voltage contains an additional term called the topological Hall effect.[13] This effect occurs when an electron passes through a skyrmion. The skyrmion can act as a magnetic flux, causing the electron to pick up a Berry phase and, essentially, be exposed to an effective electromagnetic field.[12]

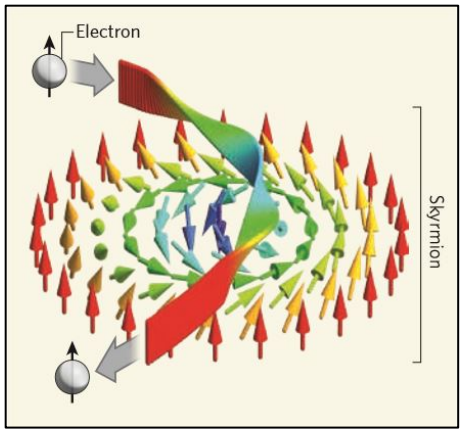

Source: Pfleiderer, C. & Rosch, A. Condensed-matter physics: Single skyrmions spotted. Nature 465, 880–881 (2010)

When a threshold current density is reached, the skyrmion will experience depinning by accepting the spin transfer torque from the electrons, thus causing the skyrmion to drift in two directions: parallel to the current, which is the more dominant term, and opposite to the electron Hall current.[4,12] The flow of skyrmion crystals has in fact been shown to give rise to an altered Hall resistivity at different current densities.[4] This project analyzes the topological Hall resistivity at multiple temperatures, current densities, and film thicknesses in order to determine whether skyrmions in FeGe are feasible for use in magnetic information storage.

II. Methods

- **Sputter deposition of FeGe films:**

FeGe thin films were grown epitaxially using off-axis magnetron sputtering. The sputtering system consists of an ultrahigh vacuum chamber that utilizes Ar as its sputtering gas.

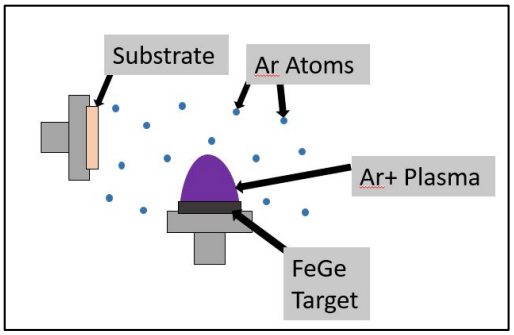

A direct-current (DC) voltage is applied to a target material, which causes the electrons near the surface of the material to ionize the Ar atoms, forming Ar^+ ions. Because of the electric field caused by the DC voltage, the Ar^+ ions are attracted to the target. In addition, magnets are placed behind the target to create a magnetic field, causing the Ar^+ to spiral perpendicularly to the target's normal, bombarding the target and blasting off atoms from its surface. Some of these atoms will travel towards the substrate, sticking to its surface and forming a film. If a substrate of matching crystal structure and lattice constants is used and heated to an appropriate temperature, an epitaxial film can be grown.

In this particular study, off-axis magnetron sputtering was used. This means that the normals of the target and the substrate are perpendicular to each other. The advantage to this method is that the sputtered atoms are at a lower kinetic energy than in other methods (e.g. on-axis magnetron sputtering). This is critical to epitaxial film growth, as atoms with high kinetic energy can cause defects in the film. Additionally, epitaxial growth of FeGe requires a heated substrate because the sputtered elements are allowed to diffuse across the substrate to form the crystal.

In order to obtain a high quality sample, some steps must be taken to ensure that the substrate is prepared properly for growth. In this experiment, a Si (111) substrate is used because the lattice constant of Si (111) matches well with that of B20-phase FeGe, which is optimal for epitaxial growth. The substrate is first wiped clean with a solvent, such as methanol. Next, the substrate is dipped into a buffered hydrofluoric acid solution for 30 seconds to etch away surface dioxide, followed by rinsing in distilled water to remove the acid. Nitrogen gas is then used to blow dry the wafer. The substrate is now prepared for sputtering.

- **X-Ray Diffraction:**

X-ray diffraction is a standard technique in determining the crystal lattice constant and the quality of an epitaxial thin film. In X-ray diffraction, a monochromatic plane wave of X-rays is incident on a sample surface with certain crystal structure(s) at an incidence angle θ to the sample surface. The X-rays will reflect from the sample at an angle 2θ from the initial direction of propagation. Considering the first and second atomic planes on the sample surface, the X-rays that reflect from the first atomic plane travel a distance of $2d\sin\theta$ shorter than the X-rays that reflect off of the second plane, where d is the distance between the two adjacent atomic planes. According to Bragg's Law, constructive interference will occur if the path difference is equal to an integer multiple of the wavelength λ of the X-rays.

$$n\lambda = 2d\sin\theta \qquad (1)$$

This is the basis for X-ray diffraction. The distance between the atomic planes for B20-phase FeGe is known. Thus, by placing the detector at the theoretical angle of reflection and performing a rocking curve, the uniformity of the crystal can be determined based on the width of the detected peak. Additionally, a broader scan of angles can be performed in order

to ensure that no unwanted phases are present in the crystal. In particular, FeGe crystals can exist in both the B20 phase and the B35 phase. Using X-ray diffraction, we can show that only the B20 phase is present in the sample.

- **Hall Measurements:**

The next step is to measure the Hall effect of the sample. Two separate devices were used to measure the Hall effect: a Quantum Design Superconducting Interface Device (SQUID) magnetometer and a Quantum Design Physical Property Measurement System (PPMS). Optical lithography was used to pattern Hall bars on the FeGe films.

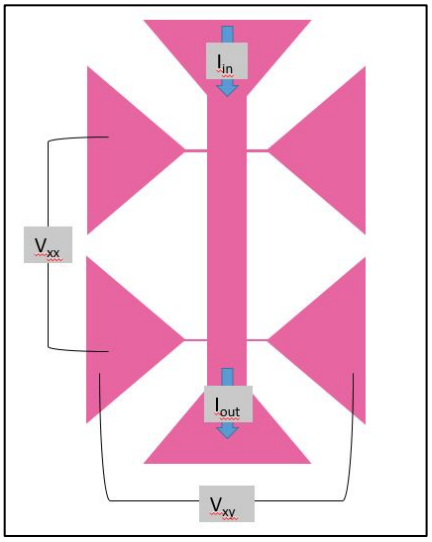

The PPMS simultaneously measures the longitudinal resistance and the Hall resistance. A current is passed through the two current leads across the central path of the Hall bar while the two inner leads measure the voltage produced to determine longitudinal resistance and the two transverse leads measure the Hall voltage. The longitudinal and Hall resistivity of the sample can be calculated from the voltages. In this experiment, the current density and the temperature are varied in order to determine the optimal parameters for skyrmion formation. The constant current density is applied using a current source meter. Additionally, the voltages were measured using a nanovoltmeter or a lock-in amplifier.

The lock-in technique is crucial to measuring the voltage at low current densities. In this situation, measurements at very low current densities are difficult to observe due to noise which can be significantly reduced using lock-in amplification.

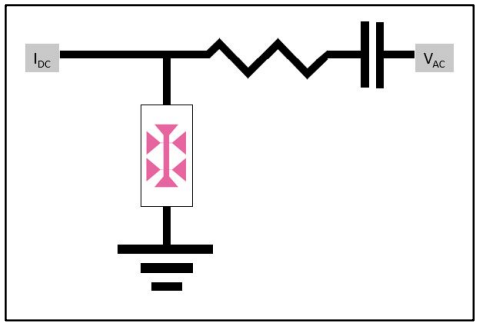

This method involves combining an AC current with a DC current, where the DC current is much larger than the AC current. The amplitude of the AC current is only a few percent of that of the DC current. Initially, an AC voltage and DC current are produced. The AC voltage is passed through a capacitor and resistor, which produces an AC current. This current is then combined with a DC current that is produced by a Keithley 2400 SourceMeter, and the combined signal is passed through the sample. The resulting current is then passed to a lock-in amplifier, the Stanford Research Systems SR830, which takes advantage of phase-sensitive detection (PSD). PSD is what allows for the true signal to be isolated from the noise. Suppose that a waveform is produced as a result of some measurement, $V_1=V_{meas}\sin(\omega_1+\theta_1)$, combined with a reference waveform, $V_2=V_{ref}\sin(\omega_2+\theta_2)$. The result of the phase sensitive detection is a multiplication of these two waves,

$$V_{PSD} = V_1 V_2$$
$$= V_{meas}V_{ref}\sin(\omega_1 t+\theta_1)\sin(\omega_2 t+\theta_2)$$
$$= \frac{1}{2}V_{meas}V_{ref}\cos((\omega_1-\omega_2)t+\theta_1-\theta_2) - \frac{1}{2}V_{meas}V_{ref}\cos((\omega_1-\omega_2)t+\theta_1+\theta_2) \quad (2)$$

If ω_1 and ω_2 are equal to each other, then the first term is a DC signal. The output from the PSD is then sent through a low pass filter, which will remove any AC signal, including both the second term and the noise from the measured voltage. The remaining output is

$$V_{PSD} = \frac{1}{2}V_{meas}V_{ref}\cos(\theta_1-\theta_2) \quad (3)$$

Assuming that the reference is in phase with the load voltage, then it is a simple matter to isolate the true signal. This signal is then passed to a nanovoltmeter for measurement.

The other major piece of equipment used to measure the Hall effect is a SQUID magnetometer. This takes advantage of Faraday's law and sensitive superconductor Josephson junctions to measure the magnetization of a material. A superconducting ring has a current passed through it that acts as a standard. The sample is then lowered through the ring, which, according to Faraday's law, induces a current and a voltage in the ring. One half of the ring will experience an increase in current while the other half experiences a decrease. The magnetization of the material can then be determined based on the difference in current and voltage between each side of the ring.

All of these measurements contribute to determining the topological Hall effect. The total Hall resistivity is a combination of three terms: the ordinary Hall resistivity, the anomalous Hall resistivity, and the topological Hall resistivity

$$\rho_{xy} = \rho_{OH} + \rho_{AH} + \rho_{TH} = R_oH + R_sM + \rho_{TH} \quad (4)$$

In order to obtain the topological Hall resistivity, the other two terms are subtracted from the total Hall resistivity, ρ_{xy}. The anomalous Hall coefficient, R_s, can be exchanged using a power-law form of ρ_{xx}, $R_s = b\rho_{xx}^2 + c\rho_{xx}$. This term can be substituted into equation (4). However, measurements have shown that the linear term, ρ_{xx}, can be neglected. More specifically, a plot of $\log\rho_{AH}$ vs. $\log\rho_{xx}$ displays a slope of 2.3, leading to the conclusion that the squared term dominates. Thus, the equation reads

$$\rho_{xy} = R_oH + b\rho_{xx}^2M_s + \rho_{TH} \quad (5)$$

By selecting high magnetic fields that do not allow skyrmion to exists, the remaining unknowns, R_o and b, can be determined. Removing the topological term leaves

$$\frac{\rho_{xy}}{H} = Ro + \frac{b\rho_{xx}^2M_s}{H} \quad (6)$$

Thus, setting up a linear plot will leave R_o and b as the y-intercept and slope. Now, all terms in equation (4) are known other than the topological Hall resistivity, and so subtracting the ordinary and anomalous Hall resistivities from the total Hall resistivity will yield the topological Hall resistivity.

III. Results and Discussion

From Equation (5), the directly observable quantities are ρ_{xx}, ρ_{xy}, M, and H. The ordinary Hall coefficient, R_o, and b are obtained through data analysis. The total Hall resistivity can be measured using the PPMS. Due to time constraints, the results displayed below were obtained prior to implementation of the lock-in amplification technique. A current is passed through the sample while the transverse voltage, V_{xy}, is measured.

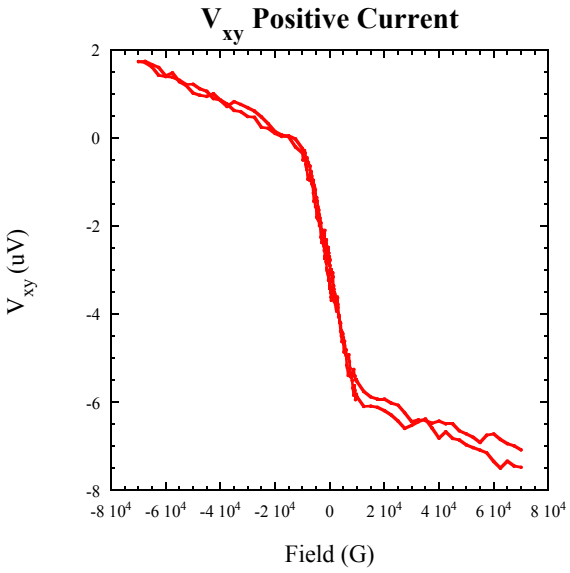

However, there is some background interference due to temperature gradients at various electric junctions and intrinsic electrical noise. Temperature gradient components of the plot are removed by reversing the current direction and measuring the same quantity.

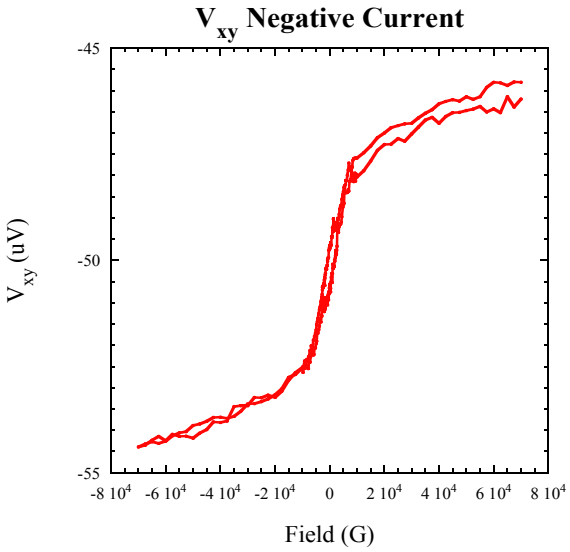

The negative current plot is combined with the positive current plot, and then divided in half. After averaging the two transverse voltages, the result is multiplied by a constant, yielding the total Hall resistivity, ρ_{xy}. It is important to note that the value of the Hall resistivity is slightly negative at zero field when sweeping from a positive field to a negative field. This will be important later in proving that there must be some term, other than the ordinary and anomalous Hall effects, that influences the total Hall resistivity.

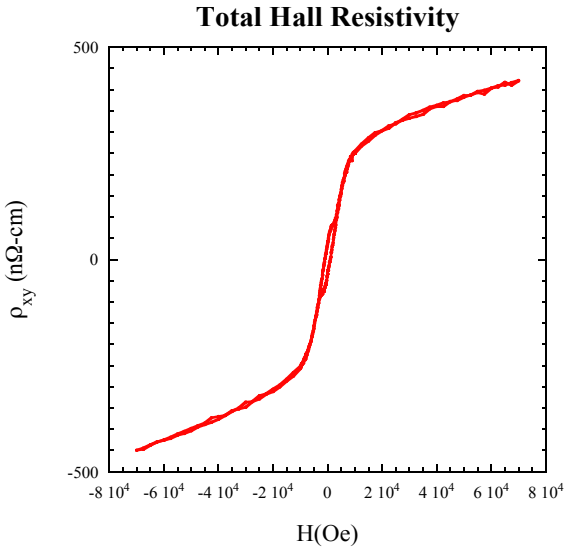

To realize the linear relationship mentioned above, the longitudinal resistivity and the magnetization must be measured. The longitudinal voltage may be measured in the PPMS simultaneously with the transverse voltage. Just as was done for the combined transverse voltage, the longitudinal voltage is converted to obtain the longitudinal resistivity, ρ_{xx}.

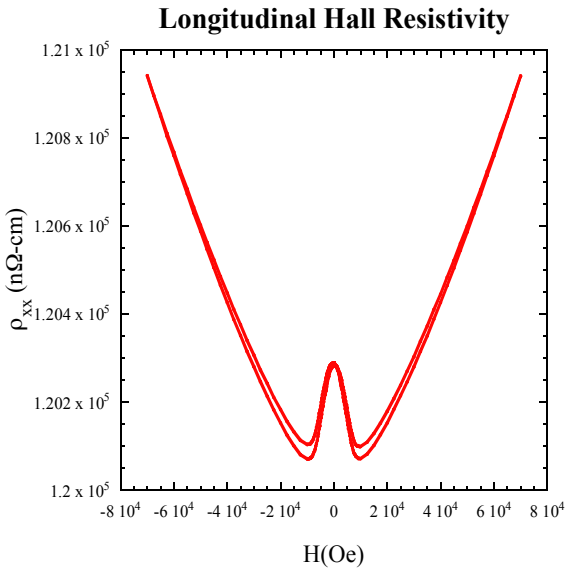

The final term needed, the magnetization, is measured using the SQUID magnetometer.

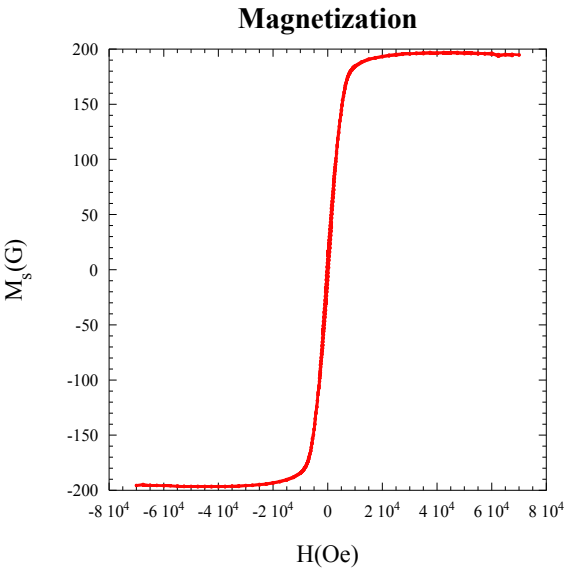

Now, the aforementioned linear plot may be established. It has been shown in previous work that the topological Hall effect becomes negligible at fields larger than 2 T. Thus, to determine the values of R_o and b, only values obtained from fields where $|H| \geq 2$ T are considered for this plot.

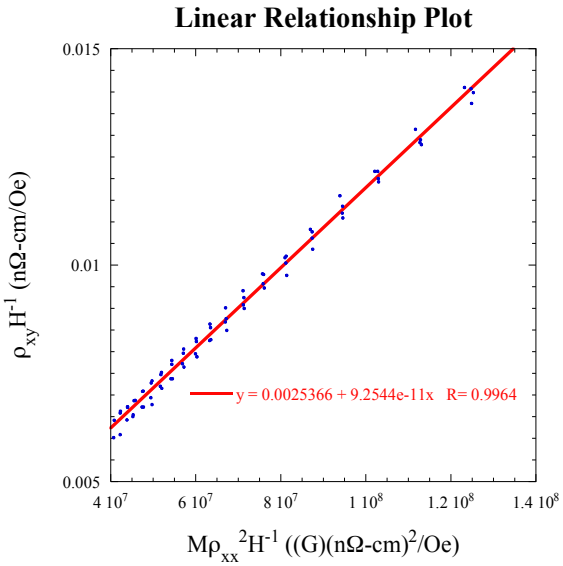

In this case, the value of b is 9.2544 nΩ-cm/Oe, and the value of the ordinary Hall coefficient, R_o, is 0.00254 1/(G)(nΩ-cm). From this, the ordinary and anomalous Hall resistivities are realized.

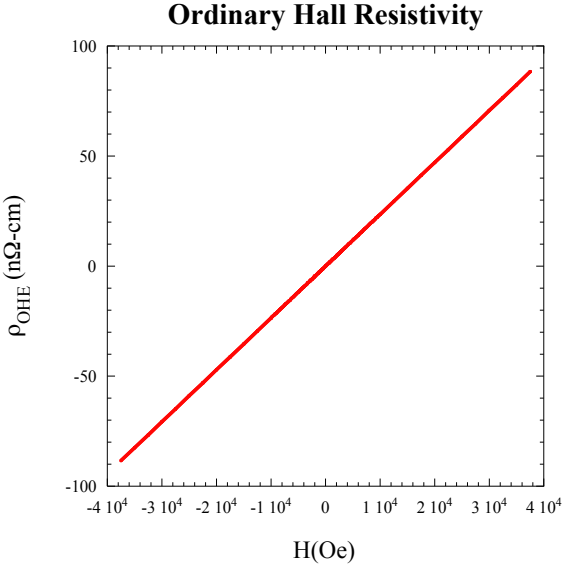

Anomalous Hall Resistivity

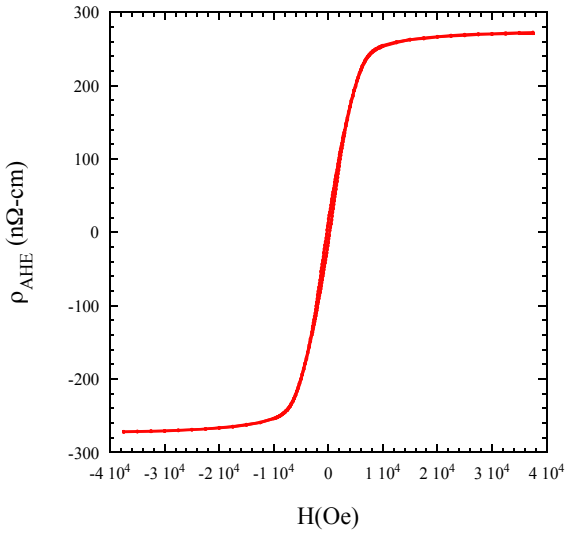

Note that the plot of the anomalous Hall resistivity crosses the x-axis with a positive value. However, the total Hall resistivity was shown to cross the x-axis slightly below zero. The ordinary Hall resistivity is 0, so it does not cause this change in the total resistivity. Thus, it can be concluded that there must be another term that dominates around the zero field domain. This term is the topological Hall resistivity, which can be extracted by subtracting the ordinary and anomalous Hall resistivities from the total Hall resistivity.

Topological Hall Resistivity

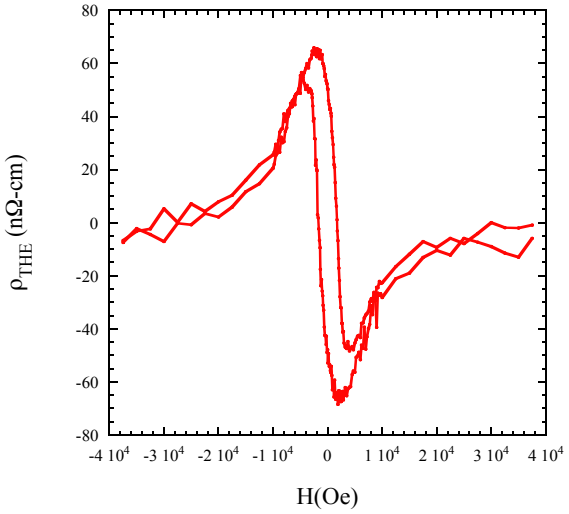

These measurements were carried out for two different film thicknesses, at varying temperatures and current densities. The following four plots were created in order to determine the dependence of the topological Hall resistivity on those three parameters.

Temperature Dependence (80 nm, 80uA)

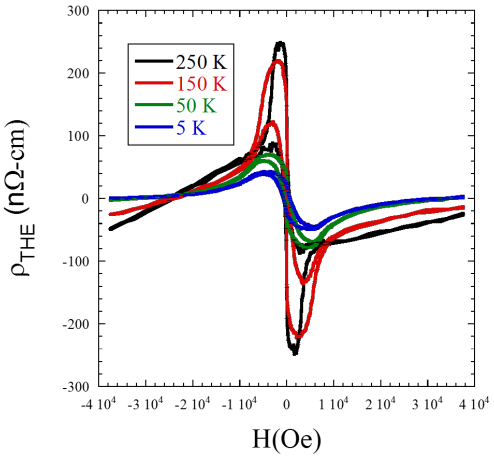

Based on these results, the topological Hall resistivity increases with increasing temperature. It is important to note that there should be some critical temperature below which skyrmions are formed. This would be exemplified in the graph as a decreased effect at temperatures lower than the

critical temperature. Because this result is not observed, it is concluded that the critical temperature must be greater than 250 K.

Current Dependence (40 nm, 50 K)

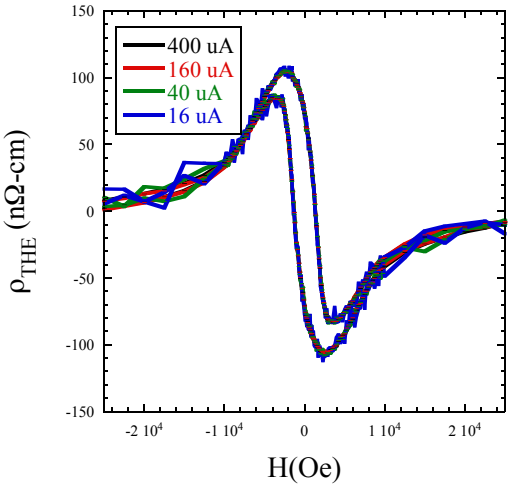

Analyzing the dependence of the current density reveals that there is no current dependence; the same results are achieved at all currents. Theoretically, there should be a critical current at which all greater currents will yield similar topological Hall resistivities and all lower currents will yield similar results. This current is not observed in these measurements. It is possible that the critical current density is lower than that of the observed values, thus further measurements which utilize the lock-in technique should expose the critical current density.

Thickness Dependence (16 uA, 50 K)

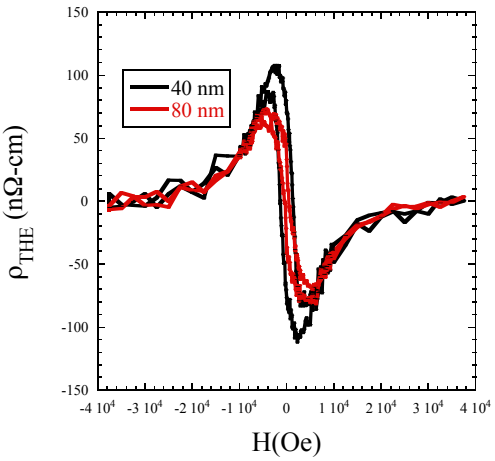

Thickness Dependence (16 uA, 200 K)

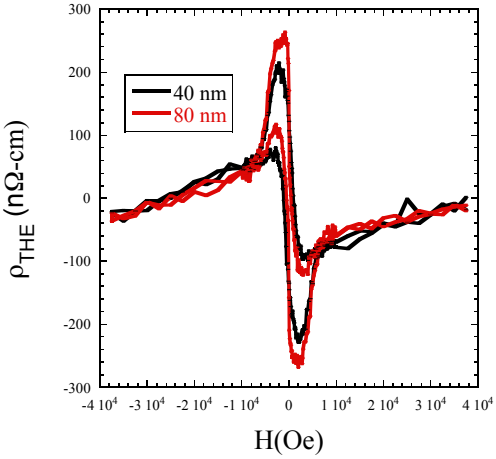

The data above shows the thickness dependence of the topological Hall resistivity for two thicknesses: 40 nm and 80 nm. At 50 K, the thinner sample displays a larger topological Hall resistivity than the thicker sample. However, at a larger temperature (200 K), the thicker sample yields a larger effect than the thinner sample. This can be explained by returning to the phase diagram of the skyrmion phase in FeGe films. The 200 K measurement seems to be located in the middle of the skyrmion phase for both the 80 nm and 40 nm samples. However, the 50 K results are only in the center of the skyrmion phase for the 40 nm sample. For the 80 nm sample, the temperature leads to a location on the phase diagram that is

most likely a transition phase where some skyrmions appear, but it is not located in the center of the skyrmion phase. It is important to note that it may be possible for the phase diagram to be dependent on the growth method of the films.

IV. Conclusions

This project reports on the temperature, current density, and thickness dependence of the topological Hall resistivity in FeGe thin films. It was shown that the topological Hall resistivity increases with increasing temperature, that there is no current density dependence, and that the thickness dependence also depends on the location in the skyrmion phase of the phase diagram.

In the future, measurements should be put towards further analyzing the critical current density using the lock-in technique. Additionally, the thickness dependence should be investigated using a larger amount of thicknesses while taking the skyrmion phase diagram into account in order to obtain the best results.

V. Acknowledgments

This work was supported by NSF Award Number DMR-1420451 through the REU program which is part of an NSF Materials Research Science and Engineering Center. The Ohio State University Department of Physics and Center of Emergent Materials are acknowledged for hosting this project and providing the equipment and resources needed to carry out these measurements.

VI. References

1. Nagaosa, N. & Tokura, Y. Topological properties and dynamics of magnetic skyrmions. Nat. Nanotechnol. 8, 899–911 (2013).
2. Li, Y. et al. Robust Formation of Skyrmions and Topological Hall Effect Anomaly in Epitaxial Thin Films of MnSi. Phys. Rev. Lett. 110, 117202 (2013).
3. Romming, N. et al. Writing and Deleting Single Magnetic Skyrmions. Science 341, 636–639 (2013).
4. Yu, X. Z. et al. Skyrmion flow near room temperature in an ultralow current density. Nat. Commun. 3, 988 (2012).
5. Grigoriev, S. V. et al. Helical spin structure of Mn1−yFeySi under a magnetic field: Small angle neutron diffraction study. Phys. Rev. B 79, 144417 (2009).
6. Grigoriev, S. V. et al. Magnetic structure of Fe1−xCoxSi in a magnetic field studied via small angle polarized neutron diffraction. Phys. Rev. B 76, 224424 (2007).
7. Yu, X. Z. et al. Near room-temperature formation of a skyrmion crystal in thin-films of the helimagnet FeGe. Nat. Mater. 10, 106–109 (2011).
8. Shibata, K. et al. Towards control of the size and helicity of skyrmions in helimagnetic alloys by spin–orbit coupling. Nat. Nanotechnol. 8, 723–728 (2013).
9. Kanazawa, N. et al. Large Topological Hall Effect in a Short-Period Helimagnet MnGe. Phys. Rev. Lett. 106, 156603 (2011).
10. Moriya, T. Anisotropic Superexchange Interaction and Weak Ferromagnetism. Phys. Rev. 120, 91–98 (1960)
11. Dzyaloshinsky, I. A thermodynamic theory of 'weak' ferromagnetism of antiferromagnetics. J. Phys. Chem. Solids 4, 241–255 (1958).
12. Schulz, T. et al. Emergent electrodynamics of skyrmions in a chiral magnet. Nat. Phys. 8, 301– 304 (2012).
13. Pfleiderer, C. & Rosch, A. Condensed-matter physics: Single skyrmions spotted. Nature 465, 880–881 (2010)

Proximity Induced Ferromagnetism in Pt|$CoFe_2O_4$ Hybrid Interfaces

Adam Z. Goad[1], Igor Pinchuk[2], Walid Amamou[3], Roland Kawakami[2,3]
[1]University of Maryland, Baltimore County,
[2]The Ohio State University, [3]University of California, Riverside

ABSTRACT

Manipulation of electron spin is essential to unlocking the potential of spin-based logic devices for information processing. Inducing magnetism within nonmagnetic materials by means of a proximity effect will enable us to more definitively and effectively manipulate electron spin within a system. With our project, we are looking to report evidence of proximity induced ferromagnetism in a thin film of Pt covering a ferromagnetic insulator, $CoFe_2O_4$. Hall bars are created to enable us to make Hall measurement of the induced ferromagnetic Pt thin film. If an anomalous hall effect is present in the Pt thin film, evident of proximity induced ferromagnetism, then we will see a non-linear relationship between the measured Hall voltage and the applied magnetic field. When we have confirmed the presence of proximity induced ferromagnetism in a nonmagnetic thin film, we can attempt to tune the effect. By taking Hall measurements of Hall bars with different termination layers, we may be able to control the presence and even magnitude of our observed induced magnetism. If we can verify proximity induced ferromagnetism in thin films, then we can pursue verification of proximity induced ferromagnetism in two-dimensional (2D) materials. The possibilities of 2D materials are bountiful, but if we are able to exhibit proximity induced ferromagnetism in them, we can unlock the possibilities of 2D materials that are limited by non-magnetism.

I. Background and Introduction

The manipulation of electron spin through controlled magnetization of materials has amassed much attention recently from scientists in the field of electronics. Mastery of the electron spin degree of freedom could enable optimization of electronic devices used for information processing. The development of spin-logic devices has long been anticipated as additions and replacements to current information processing devices. There are many avenues to approaching the goal of controlled magnetization of materials. One of those avenues is the proximity effect. Through the proximity effect, we can induce magnetism into materials that are not innately magnetic. Proximity induced ferromagnetism from insulating films of $CoFe_2O_4$ will provide the avenue to introduce and control the magnetization of metallic ultrathin films.

Induced magnetism has been shown previously in various systems. Recently, YIG was used to induce magnetism in thin films of Pt. YIG was successful in manipulating the magnetization of the Pt, yet YIG is a soft magnet. YIG's soft magnetic properties prove to be unsatisfying for electronic applications because YIG can be easily remagnetized and corrupted. To combat this issue, the obvious choice is an equally effective hard magnetic material, CoFe2O4. Insulating spinel ferrites

($CoFe_2O_4$, $NiFe_2O_4$, ect.) could unlock the possibilities of sustainable proximity induced ferromagnetism in metallic thin films. Pt thin films are used as the nonmagnetic conductor because they nearly satisfy the Stoner criterion to enter a ferromagnetic state and Pt's relatively large mass results in a nontrivial spin orbit interaction, which generates an easily distinguishable anomalous Hall signature, should Pt become ferromagnetic.

In order to prove proximity induced ferromagnetism of a Pt thin film on $CoFe_2O_4$, we performed Hall measurements on Molecular Beam Epitaxy (MBE) grown Pt|$CoFe_2O_4$ Hall bars that we fabricated through a resist, development, and ion milling process. From the Physical Properties Measurement System (PPMS) derived Hall measurements, there is a consistent and distinct signature of the anomalous Hall effect, indicative of magnetic moments present within a material. When the linear background of the standard Hall effect is subtracted from the data set, the clear anomalous trend is observed around the zero applied magnetic field point. Otherwise, the measured voltage follows a linear trend until it saturates near the limits of the magnetic field domain. Therefore, with the evidence of the anomalous Hall effect in the measure Pt thin film, we can confidently conclude that $CoFe_2O_4$ is utilizing the proximity effect to induce ferromagnetism to Pt thin films.

The implications of our results with induced ferromagnetization of Pt could introduce 2D materials (such as graphene) to the proximity effect. If magnetization of 2D materials can be harnessed by the proximity effect, these magnetic 2D will prove to be monumental additions to the field of Spintronics.

II. Methods

In this study, 10 x 10 x 0.5mm MgO(001) double-sided polished substrates were rinsed in deionized water and loaded into a UHV chamber with a base pressure of ~$2x10^{-10}$ torr. Prior to deposition of CFO films, the substrate surface is cleaned by annealing at 600˚C for 30 minutes and smoothed by subsequent deposition of ~5nm electron beam MgO buffer layer grown at 350˚C at a rate of 1 Å/min. Growth temperatures and deposition rates are measured by a thermocouple placed near the substrate and a quartz crystal monitor respectively. CFO films were deposited at ~4 Å/min in an oxygen partial pressure of $5x10^{-7}$ torr by co-depositing elemental Co (99.99%, Alfa Aesar) and Fe (99.99%, Alfa Aesar) evaporated from thermal effusion cells.

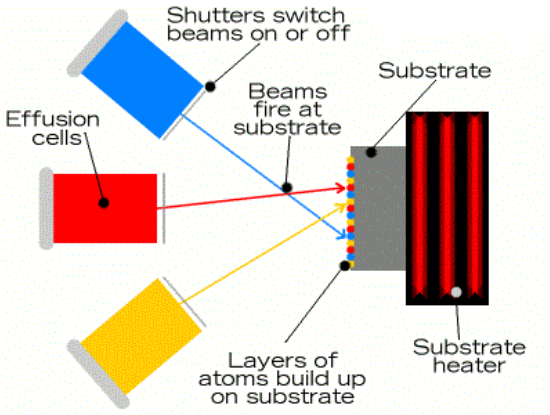

MBE Growth Schematic
http://www.explainthatstuff.com/molecular-beam-epitaxy-introduction.html

Substrate temperature was maintained at 200˚C during CFO growth and *in situ* Reflection High Energy Electron Diffraction (RHEED) was used to monitor the sample surface throughout the growth and annealing process. CFO films were then cooled to room temperature and

capped with either Pt or Al/5nm MgO/2nm Al. Pt films were deposited at ~0.2Å/min using an electron beam source while Al films were grown at 1Å/min using a thermal effusion cell. The described heterostructures were deposited without breaking UHV conditions in order to preserve the quality of the CFO/Pt and CFO/Al interface.

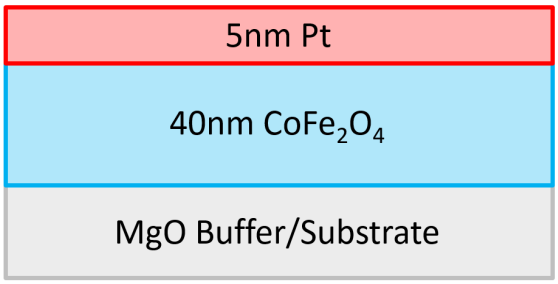

Growth structure of Pt|$CoFe_2O_4$ sample.

Magnetization measurements were performed at various temperatures using a Quantum Design 14 Tesla Physical Properties Measurement System (PPMS) with a Vibrating Sample Magnetometer (VSM) module. The MgO/Pt, MgO/CFO/Pt and MgO/CFO/Al samples were patterned into Hall bars (W=100μm, L = 800μm) for subsequent DC magnetoresistance and Hall measurements. DC transport measurements with obtained in the same PPMS using a resistivity module.

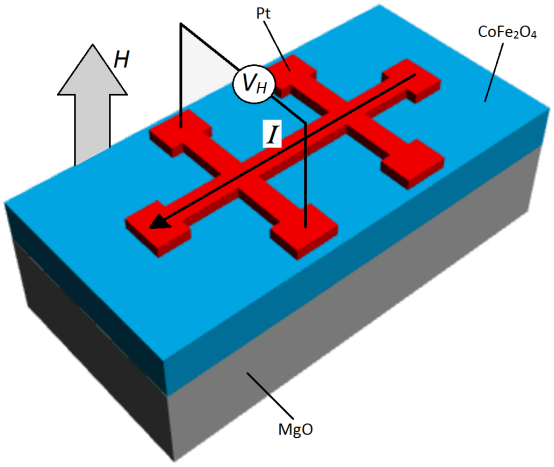

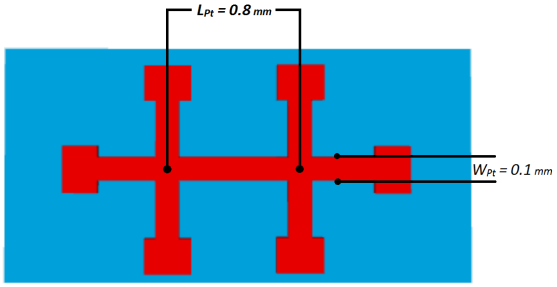

Hall bars are fabricated using a polymer resist, laser writing, chemical development, and ion milling process. Hall measurements are taken using PPMS. **Top**: 3D view of Pt|$CoFe_2O_4$ Hall bar undergoing a Hall measurement. **Bottom**: Top view of Pt|$CoFe_2O_4$ Hall bar with dimension specifications.

III. Results and Conclusions

First, we characterize the growth of $CoFe_2O_4$ using RHEED as we codeposit Co and Fe in oxygen environment of $5x10^{-7}$ Torr. The RHEED patterns are taken along [100] and [110] incident crystal directions of MgO buffer layer and 40nm CFO film.

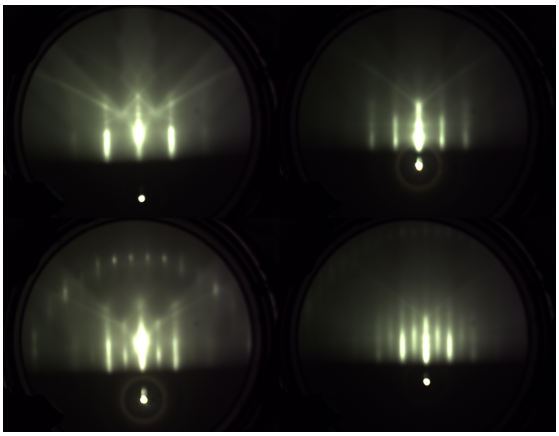

RHEED diffraction patterns show the crystallinity of the material. The diffraction pattern transition from a dull and blotchy pattern to a sharp and streaky pattern is indicative of the transition from the rough crystalline surface of MgO to the epitaxial growth of a smooth $CoFe_2O_4$ film. All images taken at sample temperature 200C. ***Top Left and Right****: 5 nm MgO (100) and (110), respectively, buffer layer on MgO substrate.* ***Bottom Left and Right****: 40 nm $CoFe_2O_4$ (100) and (110), respectively, on 5 nm MgO buffer layer.*

Both images display sharp and streaky diffraction maxima, indicating flat and single crystal surfaces on ~100nm scale corresponding to the coherence length of RHEED. The spacing between diffraction maxima of MgO pattern is twice as large as that of CFO, consistent with the expectation that real space lattice constant of MgO (4.21Å) is half as large as that of CFO (8.39Å). This is confirmed by θ-2θ x-ray diffraction spectrum of the film, resolving clear MgO and CFO peaks.

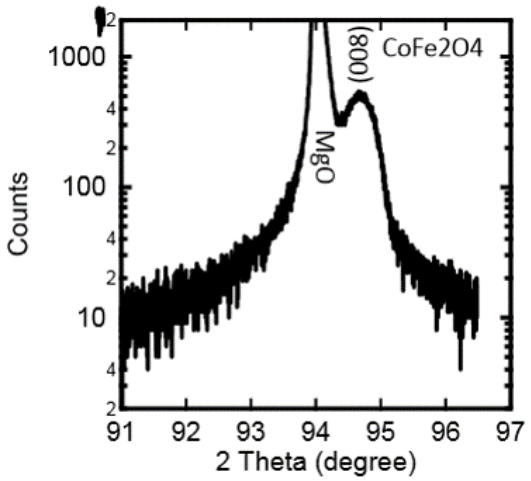

XRD diffraction intensity counts.

To check the morphology of our film, we perform Atomic Force Microscopy (AFM) on the as grown $CoFe_2O_4$ immediately after growth. The AFM scans over the area of 5μm x 5 μm. The film exhibits a very smooth surface over large area with a mean roughness of 0.06 nm over 5μm x 5 μm scan.. These results confirm the high crystallinity of the MBE-deposited CFO films with a smooth Pt/CFO interface, which is a key toward obtaining magnetic proximity effect.

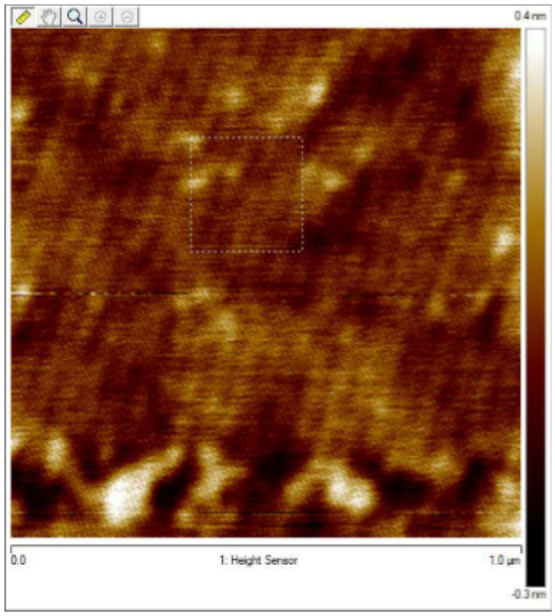

AFM scan of Pt|$CoFe_2O_4$ sample

The magnetization loop of Pt (5 nm)/CFO (40nm)/MgO structure at room temperature and 10 K where the magnetic field is applied out-of-plane is shown below. The saturation field of the CFO at low temperature (10K) is corresponding to a net magnetic moment of 2.5μ_b per formula unit. We observe a large coercive field of H_c = 2500 Oe and remnant out of plane magnetization of M_r/M_s.

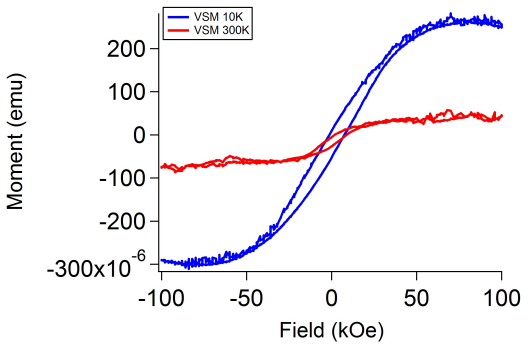

VSM measurements of $CoFe_2O_4$ at 10 K and 300 K.

One important feature in all of our measured magnetization loops is the absence of antiphase boundaries (APBs) usually characterized by a sharp decrease of the total magnetization close to zero

field and smaller coercive fields. Instead we observe a smooth hysteresis loop over the whole range of the applied magnetic field. This suggests that our films are free of defects at the interface.

In the following paragraphs we present the central result of the paper that is the demonstration of magnetic proximity effect in Pt using the Anomalous Hall Effect (AHE) measurement.

To perform the Hall measurements, we apply an out of plane magnetic field as we measure the transverse $R_{xy}=V_{xy}/I$ and longitudinal resistance $R_{xx}= V_{xx}/I$ where I=50 uA for the injected current and $V_{xy,xx}$ is the measured voltage. We measured Hall Effect in Pt/MgO, MgO/CFO/Al and MgO/CFOPt structures. Both MgO/Pt and MgO/CFO/Al sample shows a linear Hall background as expected for an ordinary Hall effect. In contrast, the MgO/CFO/Pt sample exhibits both the ordinary Hall effect and the anomalous Hall effect characterized by the nonlinearity of the hall signal superimposed to a linear background. Furthermore, we observe a hysteretic nonlinear background as we sweep the field in both directions which is a key characteristics of the underlying CFO substrate. After subtraction of the ordinary hall background, the hysteresis of the anomalous hall signal shows a clear saturation corresponding to the same saturation magnetization of the CFO substrate.

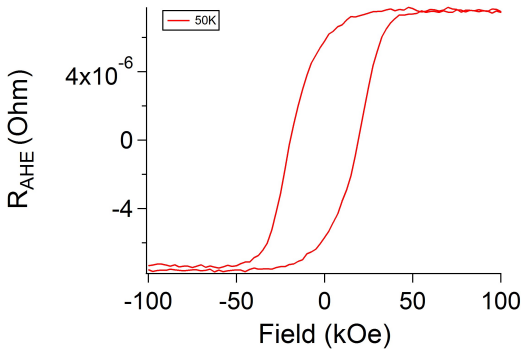

PPMS Hall measurements of Pt|$CoFe_2O_4$ Hall bar.

It is worth noting, that the coercive field of the anomalous hall signal is significantly larger than the underlying CFO substrate. Nevertheless, our results suggest the presence of strong magnetic proximity effect in the Pt layer. A clear unambiguous distinction between the ordinary Hall effect and the anomalous Hall effect is the temperature dependence.

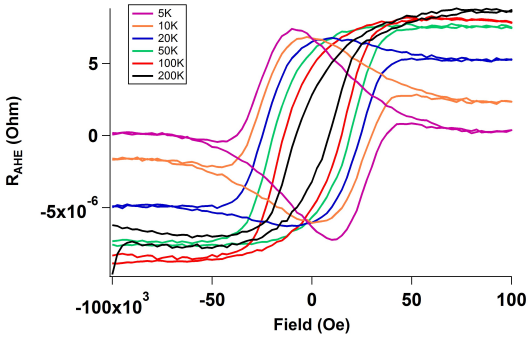

Temperature dependence PPMS measurements of Pt|$CoFe_2O_4$ Hall bar.

Our anomalous hall signal on Pt/CFO exhibits a strong temperature dependence where the signal increases at low temperature but decreases to a finite value at room temperature. These results provide a clear, unambiguous evidence of ferromagnetism induced in the Pt layer through magnetic proximity with the underlying $CoFe_2O_4$ substrate.

V. Acknowledgments

This work was supported by NSF Award Number DMR-1420451 through the REU program which is part of an NSF Materials Research Science and Engineering Center. The Ohio State University Department of Physics, Center of Emergent Materials, and Kawakami Group are acknowledged for their support and guidance in the REU process.

The Development of a Simulation model for calculating the Magnetic Field of a Complex Ferromagnetic Structure

Abstract:

The research done this summer was to solve the calculation of the magnetic field of a complex ferromagnetic structure. The method used was a "Coulombian approach". This technique uses an equivalent distribution of point charges that are within the structure and surface. The process is done by integrating small charged values distance'd' away from a point of interest. This was implemented numerically with the MatLab package. A great part of this program is the fact that I could do complex structures, which broadens its uses. The simulation is also designed to do the calculation more rapidly using numerical integration by means of MatLab and C. The code is designed to be user friendly to assist the local collaboration by comparing their experiments to the theory. For example, this code will be compared to Yttrium Iron Garnet (YIG) which is a very desirable material, because of its microwave properties.

Motivation:

Spintronics involves the manipulation of electron spins to encode data. As shown below, a ferromagnet acts as a source of precessing spins. This spin will be transferred into the neighboring non-magnetic layer. Therefore, we need to know the stray magnetic field around the ferromagnet.

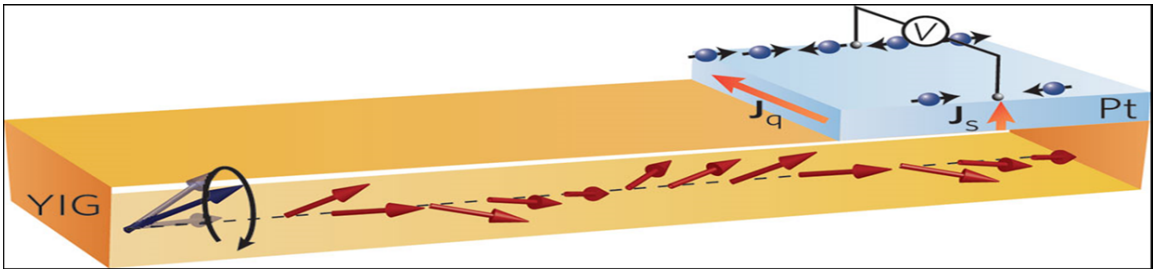

The second motivation is calculating the magnetic field of a thin film or that of a parallel plate capacitor. This shows the layout of the field when being demagnetized in the smaller direction. That the field on the top of the plates will be facing in the direction of magnetization. The field on the bottom will be direction of magnetization, but the field on the inside of the plates or film will be facing the opposite direction. This being proven correct in the simulation shows that it can be ran with the films used by the C.E.M. department.

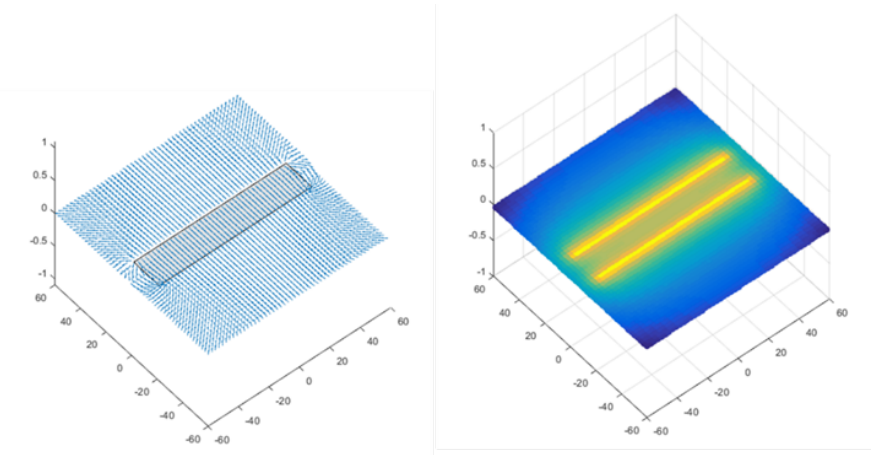

- Magnetic Slab is in xz plane
- Calculated magnetic field in xy crossection
- Panel (a): Numerically calculated magnetic field lines
- Field lines similar to that of a parallel plate capacitor
- Panel (b): Spatial dependence of log of magnetic field intensity
- Highest field intensity is observed at surfaces at position of effective magnetic charges

Background:

There are three major ways to calculate a piece of magnetic material. [1] The first is calculating the dipole field directly by integrating over the volume distribution of the magnetization. The second is use the Amp`erian approach and replace the magnetization by an equivalent distribution of current density. Then thirdly is the method I took which was the Coulombian approach and replace the magnetization by an equivalent distribution of magnetic charge. The understanding of the magnetic field of a sample such as Yttrium Iron Garnet (YIG) which is used in many applications, one of these being semiconductors which are widely used commercially. This explains why Yttrium Iron Garnet (YIG) is commonly favored to study. There are two major ways that knowing the magnetic field of an experiment. The first is the effects from your sample on certain areas or point, and the other is when the sample in which you are calculating is the one creating the magnetic field. This are just two examples where this could be the most used.

Methods:

The "Coulombian approach" replaces volume magnetization with the effective surface magnetic charges. Magnetic field at the point of interest is calculated using the Coulomb's Law for the field of a charge.

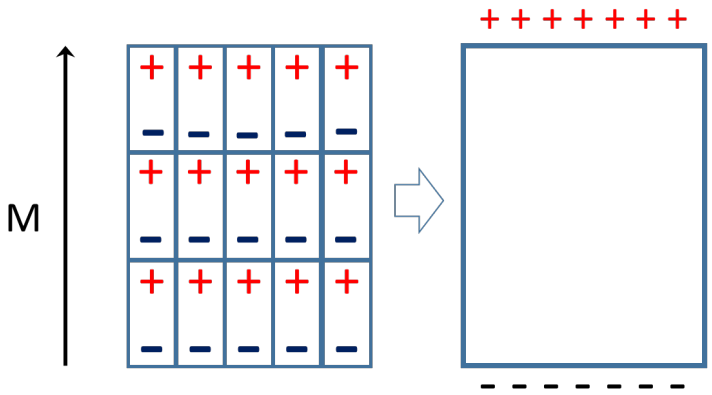

The figure above is a face of a prism showing one side as bar magnets lines up from positive to negative. The Coulombian approach uses the fact when magnetize a ferromagnetic structure the surfaces of the sample will line up leaving just the ends charged. This makes the whole prism turn into one large bar magnet. This then the prism made up from this approach are formed into another structure which then integrated over. This then calculates the magnetic field of many complex structures.

- For numerical integration over the charged surface it is approximated by an array of discrete charges $Q\_ij=\sigma\ A\_ij$ where σ is the magnetic charge density and A_ij is the area of the surface element.
- Due to the dipolar nature of magnetic field, the compensated magnetic charges always exist in pairs of surfaces with positive and negative effective magnetic charges.
- As a result the total magnetic field at the point of interest is a vector sum over the magnetic field contributions of the individual positive and negative charge elements